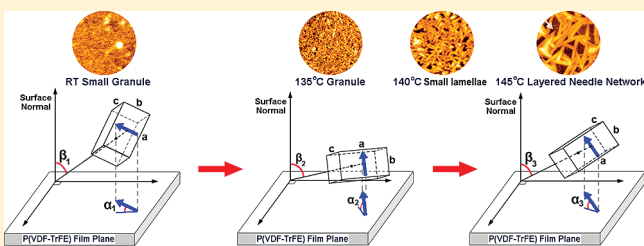


# Thermally Induced Cooperative Molecular Reorientation and Nanoscale Polarization Switching Behaviors of Ultrathin Poly(vinylidene fluoride-trifluoroethylene) Films

Dong Guo,<sup>\*†‡</sup> Igor Stolichnov,<sup>†</sup> and Nava Setter<sup>†</sup><sup>†</sup>Ceramics Laboratory, Swiss Federal Institute of Technology (EPFL), CH-1015 Lausanne, Switzerland<sup>‡</sup>Institute of Acoustics, Chinese Academy of Sciences, Beijing 100190, China

**ABSTRACT:** Ultrathin films of the ferroelectric polymer poly(vinylidene fluoride-trifluoroethylene) [P(VDF-TrFE)] have recently attracted intensive research interest due to their potential applications in emerging organic devices. As special geometry confinement systems, many aspects about their processing, microstructure, and performance are far from being well understood. Here, the cooperative molecular orientation, macroscopic ferroelectric properties, and nanoscale polarization switching behaviors of thermally crystallized ultrathin P(VDF-TrFE) films were investigated. With increasing annealing temperature, the films showed a distinct granule toward layered needle-network (LNN) morphology transition with deteriorated ferroelectricity at a critical point ( $T_{cr}$ ) around 140 °C. Accompanying this is that the polymer backbone first lay more parallel relative to the substrate, and then exactly at  $T_{cr}$  it showed an abrupt standing-up reorientation. Interestingly, the polarization axis simultaneously showed just opposite orientation and reorientation. Nanoscale polarization switching characterization by using piezoresponse force microscopy and local ferroelectric hysteresis loops revealed a varied molecular orientation in the same needle grain and a polarization reversal constraint effect by the inhomogeneous LNN structure. On the basis of these observations, a tilted-chain lamellae structural model was proposed for the LNN film. The lying down of the polarization axis and the polarization reversal constrain effect well explain the inferior performance of the LNN film despite its higher crystallinity than that of the granular film. The results may shed some light on the understanding of the intercorrelation among the thermal crystallization, microstructure, and macroscopic performance of ultrathin polymer films.



## INTRODUCTION

Because of the advantages of flexibility, large area, and low temperature processing, thin films of ferroelectric copolymer poly(vinylidene fluoride-trifluoroethylene) [P(VDF-TrFE)] have been widely used in sensors, actuators, and other microelectromechanical systems.<sup>1–4</sup> In recent years, stimulated by the rapidly developing flexible electronics industry, new organic devices based on [P(VDF-TrFE)] films such as flexible nonvolatile memories have attracted intensive research interest. Because of the huge coercive field of about 50 MV/m, “ultrathin” P(VDF-TrFE) films with a thickness thinner than 100 nm are required for attaining low voltage operation of the relevant devices. However, an ultrathin polymer film is a confinement geometry system where the mobility, crystallinity, and orientation of the polymer chains may be largely altered by special enthalpic and entropic effects at the polymer/substrate interface, and the mechanisms underlying many of its phenomena are still intensely debated.<sup>5</sup> For P(VDF-TrFE), its ultrathin films show substantially deteriorated ferroelectric properties as compared to those of thick films.<sup>6</sup> Preparation of nonleaky ultrathin films that still exhibit excellent ferroelectric properties has been an important research objective.<sup>7–9</sup> Thermal treatment is a standard procedure used in P(VDF-TrFE) film preparation for improving its electric performance. Because the ferroelectricity in the all-trans  $\beta$  phase P(VDF-TrFE) originates from F–C–H dipoles

perpendicular to the polymer backbone, analysis of the thermally induced molecular orientation change is crucial for understanding and optimizing the performance of the ultrathin films. However, crystallization of polymer is very complicated by the need of cooperative movements of the large number of connected monomers. Problems such as chain folding,<sup>10</sup> lamellar thickening,<sup>11</sup> or chain diffusion<sup>12</sup> affect molecular organization and morphologies. The situation in ultrathin films is further complicated by the constrained geometry.<sup>13</sup> As a consequence, the details of the polymer lattice orientation change upon thermal treatment and their influence on the film ferroelectric properties remain unclear, although some related results have been obtained.<sup>14–16</sup> On the other hand, to understand the fundamental nature of spontaneous order in organics and to realize the full potential of P(VDF-TrFE), significant progress must be made in understanding the ferroelectric polarization switching behavior and the possible concomitant structural change at the nanoscale. So far, only limited results have been reported concerning this,<sup>17–19</sup> although macroscopic characterizations such as dielectric measurements or pyroelectric and ferroelectric hysteresis loops have been performed extensively.

**Received:** June 29, 2011**Revised:** October 1, 2011**Published:** October 17, 2011

In particular, the correlation among the morphological features, the microscopic polarization switching, and the macroscopic ferroelectric properties of the films is still unclear.

To understand the aforementioned issues about P(VDF-TrFE) ultrathin films, in this study we report the thermally induced microstructural characteristics and their correlation with the nanoscale polarization switching behaviors and the macroscopic ferroelectric properties of spin-coated ultrathin P(VDF-TrFE) films with a thickness down to 30 nm annealed under a wide temperature range. The study was focused on films with a thickness less than 60 nm, although films of a wide thickness range were tested. It needs to be noted that ultrathin films down to one monolayer can be deposited by the Langmuir–Blodgett (LB) technique. However, the LB method is limited by the strict processing conditions and the fragility of the resulting films. Here, spin-coating is used because of its ease of operation, although it is more challenging than the Langmuir–Blodgett method in preparing ultrathin films.

## ■ EXPERIMENTAL SECTION

**Ultrathin Film Preparation and Electrical Characterization.** Highly doped bare (100) Si wafers (resistivity of 0.001–0.005 Ω cm) and 100 nm Al- and Pt-coated low doped Si wafers were used as the substrates, which were ultrasonically cleaned in acetone, isopropanol, and ultrafiltered water, and finally blown dry with nitrogen before use. Ultrathin copolymer films with a VDF/TrFE mole ratio of 70/30 (Solvay Solexis S.A.) were spin-coated on the substrates by using methyl ethyl ketone as the solvent. The film thickness was controlled by the solvent concentration. Thermal crystallization after deposition was performed for 70 min in air on a Prazitherm PZ28-2 (Harry Gestigkeit Co., Germany) precision hot plate, which has a temperature accuracy of ±0.5 °C. The hot plate was then switched off, and the samples were naturally cooled to room temperature. Metal–ferroelectric–metal capacitors were made by vacuum evaporation of 50 nm Au top electrodes on the P(VDF-TrFE) films through a shadow mask, and then polarization–electric field (*P*–*E*) loops were measured by applying a 100 Hz triangular waveform voltage to the Au top electrode while collecting the charge from the bottom electrode. All of the loops are highly reproducible and were achieved on P(VDF-TrFE) ultrathin film without any buffer layers. The leakage current was tested by a Keithley 6517 electrometer, and the data were averaged from 6 to 8 measurements on different capacitors on the same samples.

**Morphology and Microstructure Characterization.** The film morphology was inspected by a Vecco atomic force microscope (AFM) operated in noncontact mode to avoid any contact-induced structure damage or modification. The film thickness was repeatedly checked by AFM height profiles of scratches made on different areas of the same sample. Out-of-plane XRD profiles with grazing incidence geometry (op-GIXD) were recorded and compared to the normal XRD profiles of the same films by using a Bruker D8 Advance diffractometer (Cu Kα radiation, 40 kV, 40 mA). The profiles were recorded under a slow scan rate with a step size of 0.04° and a step time of 12 s, and a much slower scan with a 0.015° step size and a 24 s step time was used for the narrower range op-GIXD profiles. The macromolecular orientation was analyzed by the IRRAS (infrared reflection absorption spectroscopy) technique with a Bruker EQUINOX 55 FT-IR spectrometer equipped with a liquid nitrogen-cooled mercury cadmium telluride (MCT) detector.

The spectra were recorded using a grazing incident angle of 85° with a Spectra-tech FT 85 reflection adsorption accessory. Because films on gold are well-known to be able to produce high quality IRRAS spectra, Au-coated Si wafers were used both as the background sample and as the substrates for the film samples. 1200 scans were collected and averaged at a resolution of 2 cm<sup>-1</sup> to ensure high signal-to-noise ratios. It should be noted that, due to the large IR irradiation area under grazing incidence, rather large films with a size of 2 cm × 6 cm were used to ensure full coverage of the rectangular sampling window, and all of the spectra were obtained in the same run to rule out the influence of environment or instrument variation for different runs. These procedures are very crucial for getting high-quality IRRAS spectra.

**Nanoscale Polarization Switching and Local Ferroelectric Property Characterization.** Piezoresponse force microscopy (PFM) was carried out by the AFM equipped with a SR830 (Stanford Research Systems, Inc.) lock-in amplifier with a 2 V sine AC modulation voltage at a frequency of ~8 kHz. A soft Pt-coated AFM tip with a force constant of 0.2 N/m and a resonance constant of 13 kHz was used in PFM to avoid contact-induced morphological change. DC bias selective scanning and subsequent PFM imaging was performed to investigate the nanoscale polarization switching behavior. Local ferroelectric hysteresis loop measurement at the scale of individual grains was also carried out by the PFM facilities.

## ■ RESULTS AND DISCUSSION

**Morphology Observation.** AFM images of P(VDF-TrFE) films that have been annealed at various temperatures are shown in Figure 1. The 135 °C annealed 40 nm-thick film deposited on highly doped Si wafers (Figure 1a) consists of homogeneous small granules with a diameter in the range of 60–110 nm. The films prepared in the annealing temperature (*T*<sub>a</sub>) range of room temperature to 135 °C have a similar granular morphology (not shown), except for a gradually increased granule size with increasing *T*<sub>a</sub>. In sharp contrast, slightly increasing *T*<sub>a</sub> to 140 °C results in a film consisting of small lamellae with a width of ~120 nm and a length of 200–500 nm (Figure 1b), which suddenly transforms to a distinct needle-like network (Figure 1c) with a needle width of ~200 nm and a needle length of several micrometers when *T*<sub>a</sub> is increased to 145 °C. Beneath the needle-network, some curved “wires” with a much smaller diameter of ~70 nm could be found, as indicated by the white circle region. This reveals that the film consists of different crystalline layers with different grain growth rate. A similar needle-network with more needle grains and less wire grains was observed for a higher *T*<sub>a</sub> (Figure 1d). Some randomly distributed elliptic “melt-like” clusters can also be seen from a much larger image of the needle film (Figure 1e). The height profile in Figure 1f implies that the needles actually have a rather flat shape. More details of the film structure are reflected by Figure 2. A layered structure is much clearer in the AFM image of a thicker film shown in Figure 2a, and larger needles in the surface layers than in the lower layers can be observed. In addition, the height profile in Figure 2b reveals that each needle stem may consist of a bundle of stacked needles. Folded chain lamella is the basic structural element of semicrystalline polymers, and lamellar morphology is widely observed in polymer films. Grains with a shape similar to the needle grains shown here but with a smaller length to width ratio were also observed in P(VDF-TrFE) films,<sup>20,21</sup> while this type of grains has scarcely been reported in other polymers. The lamella

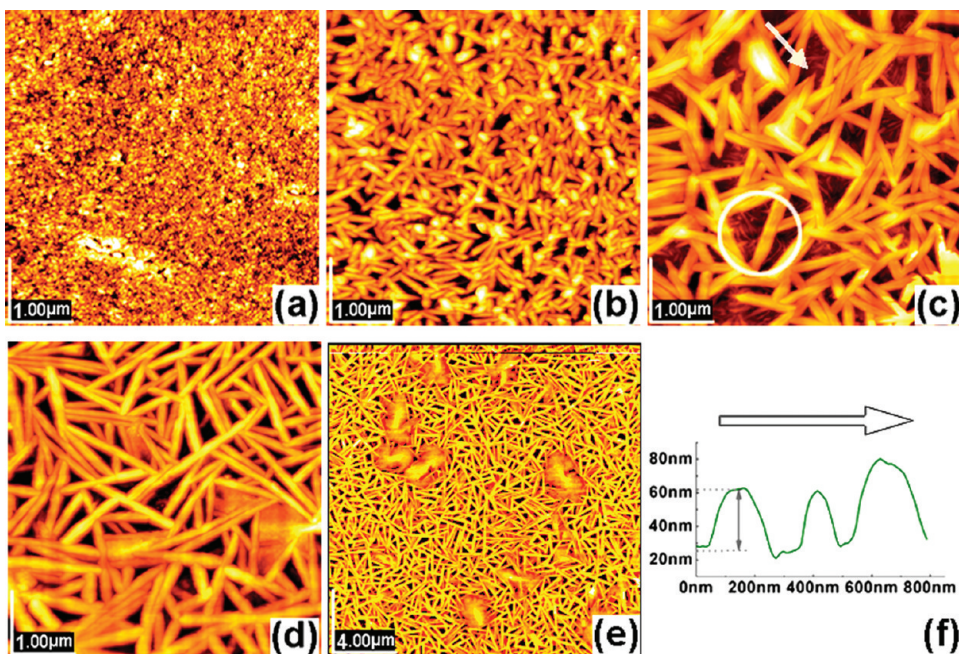


**Figure 1.** AFM images of different P(VDF-TrFE) films showing the effects of  $T_a$  on the film morphology. Parts (a), (b), (c), and (d) are 40 nm-thick films on Si annealed with a  $T_a$  of 135, 140, 145, and 150 °C, respectively. Part (e) is a  $20 \mu\text{m} \times 20 \mu\text{m}$  image of the same film shown in (c). Part (f) is the height profile along the white arrow shown in (c), which reveals the flat shape of the needle grains.

generally shows edge-on (with the backbone orientated parallel to the substrate) or flat-on (with the backbone oriented perpendicular to the substrate) grain orientation. The long narrow shape and the multiple layers of the needle grains are evidently different from those of the flat-on lamellae.<sup>22</sup> In contrast, the grains are more like edge-on lamellae, but still have a remarkable difference because the edge-on lamellae usually show a regularly packed structure with a uniform layer thickness of tens of nanometers.<sup>5</sup> A similar granule to LNN morphology transition around a critical temperature ( $T_{cr}$ ) of 140 °C was observed for all tested films with a wide thickness range of 30–250 nm on different substrates. The morphology of two typical 60 nm-thick P(VDF-TrFE) films is shown in Figures 2c and d. These indicate that the morphological features are related to the crystallization kinetics.

The nominal melting point ( $T_m$ ) of the raw P(VDF-TrFE) is 154.5 °C. However, the  $T_m$  of polymer thin film can be much lower due to the excess free energy of the folded surface of its crystals, as reflected by the Gibbs–Thomson relationship:

$$T_m = T_m^0 \left(1 - \frac{2\sigma_e}{L\Delta H}\right)$$

where  $T_m^0$  is the equilibrium melting temperature, and  $\sigma_e$ ,  $L$ , and  $\Delta H$  are the interfacial energy of the folded surface, the crystal thickness, and the heat of fusion, respectively.<sup>23</sup> Thus,  $T_{cr}$  is probably the actual  $T_m$  of the ultrathin film, and it seems reasonable to consider two different crystallization processes from the “solid” phase and from the melt at below and above  $T_{cr}$ , respectively. The much larger size of the needle grains of the samples prepared with a  $T_a$  higher than  $T_{cr}$  should have resulted from the greatly enhanced mobility of the macromolecule segments in the molten state. The layered structure may be tentatively interpreted from the viewpoint of chain mobility:<sup>24</sup>

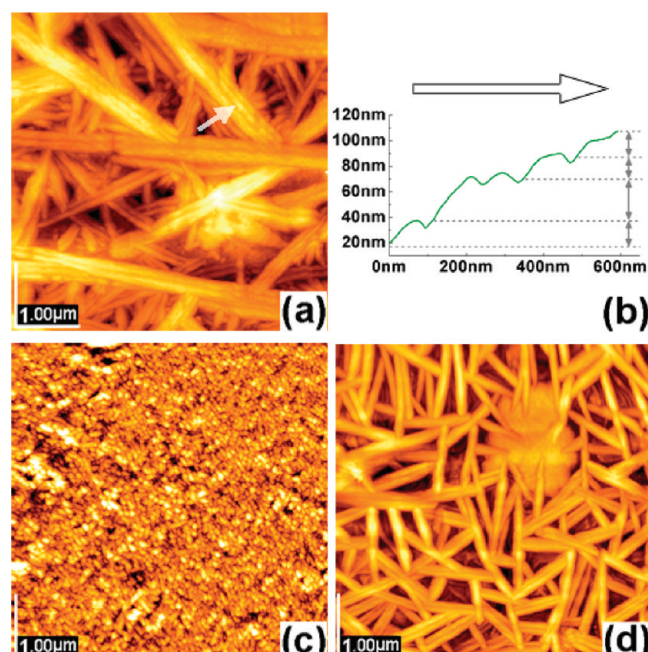


**Figure 2.** More morphology details of the P(VDF-TrFE) films. Part (a) shows the morphology of a 150 °C annealed 85 nm-thick film on Si. Part (b) is the height profile along the white arrow shown in (a), through which a layered grain structure can be seen. Parts (c) and (d) are images of 60 nm-thick films on Al-coated Si annealed with a  $T_a$  of 135 and 145 °C, respectively.

the steric constraints at the buried polymer–substrate “interface” are released at the polymer–air “free surface”, causing mobile regions around the free surface and restricted mobility regions near the interface. According to such a model, chain segments

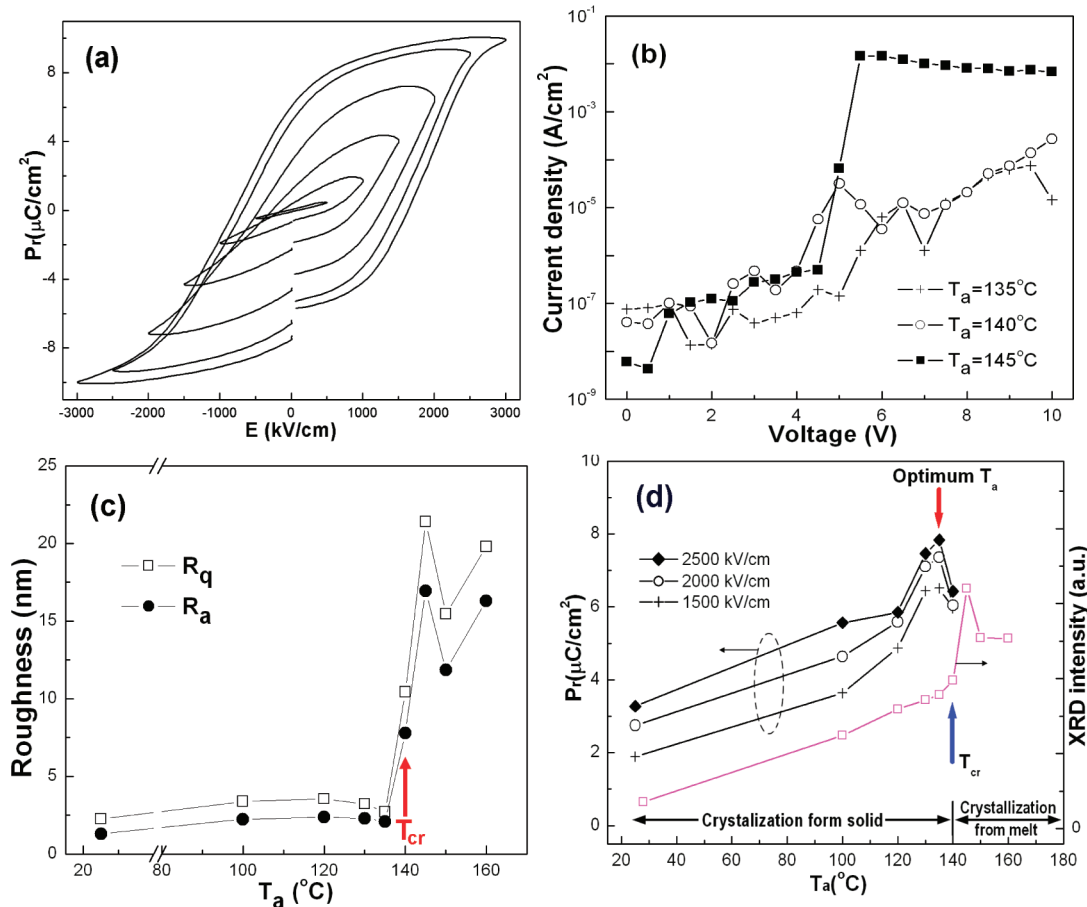


**Figure 3.** (a)  $P-E$  loops of 135 °C annealed 40 nm-thick films on Si. (b) The voltage dependence of leakage current of three typical films. (c)  $T_a$  dependence of average roughness derived from the AFM images. (d)  $T_a$  dependence of  $P_r$  and XRD intensity.

near the surface crystallize more easily than those in the proximities of the interface. Thus, at 145 °C chain rearrangement occurs preferentially at the surface, leading to grains of different size at different layers. When  $T_a$  is high enough, crystallization occurs throughout the bulk of the film, leading to more needle grains and less wire grains, with a free energy change similar to that of the "lamellae thickening".<sup>11</sup>

**Electrical Characterization.** Typical  $P-E$  loops of a 40 nm-thick granular film sample are shown in Figure 3a. The asymmetry in electric field is due to the built-in field caused by the different work functions of the top Au electrode and the Si substrate. For 40 nm-thick needle films, the leakage current was so large that the characteristic charge associated with polarization reversal was concealed and well-shaped  $P-E$  loops could not be recorded. The leakage characteristics shown in Figure 3b of three (granule, rod, and LNN) typical 40 nm-thick samples reveal that the leakage current is several orders of magnitude higher after the formation of the LNN structure when the voltage is larger than 5 V. Consistent with this is the much higher roughness of the needle film than those of the granular films shown in Figure 3c, indicating that the large amount of pinholes in the LNN film has caused the serious leakage problem. As shown in Figure 3d, both XRD intensity and remnant polarization  $P_r$  (average of  $|P_r^+|$  and  $|P_r^-|$ ) increase regularly below 135 °C. Interestingly, decreased  $P_r$  values after a maximum at 135 °C were consistently observed for films with different thickness. The formation of LNN caused deteriorated ferroelectricity, despite the improved XRD intensity.

This is clearly demonstrated by the well-shaped and reproducible  $P-E$  loops of the films prepared with a  $T_a$  around  $T_{cr}$  shown in Figure 4a-d. The round loop at  $T_a$  of 145 °C in Figure 4c also testifies to the leakage problem of the LNN films under a high voltage.

**Microstructural Characteristics.** The difficulties of polymer film structural characterization by using electron diffraction lie in the preparation of ultrathin samples that are robust enough to survive the measurement procedure. Normal XRD patterns and op-GIXD patterns of two typical 40 nm-thick films are compared in Figure 5a. The films show typical  $\beta$  phase XRD patterns with a broad peak at  $2\theta$  of ~19.7° that is attributed to the overlapped reflections from the (200) and (110) planes. In op-GIXD detector scan, the collimated incidence beam was fixed at a grazing angle of ~1°, while the detector scanned over the selected angle range. Because of the unfocused geometrical arrangement, the op-GIXD peak is much broader than the peak in the normal XRD profiles and is slightly shifted to  $2\theta = 19.5^\circ$ . The narrow peak at  $2\theta = 33.01^\circ$  in the normal XRD profiles is due to Si(100) of the substrate. The peak disappeared in the op-GIXD profiles, because the Si(100) plane is parallel to the film surface that is tilted at  $[(33.01 - 1)/2] \approx 16^\circ$  away from the diffraction plane with op-GIXD geometry. As an analogue, the peaks at  $2\theta = 19.5^\circ$  mainly reflect the diffraction intensity of the P(VDF-TrFE) lattice planes tilted ~9.25° away from the film plane. Hence, their much weaker intensity than that of the normal XRD peaks should result from the preferential lattice orientation with the {200} or {110}

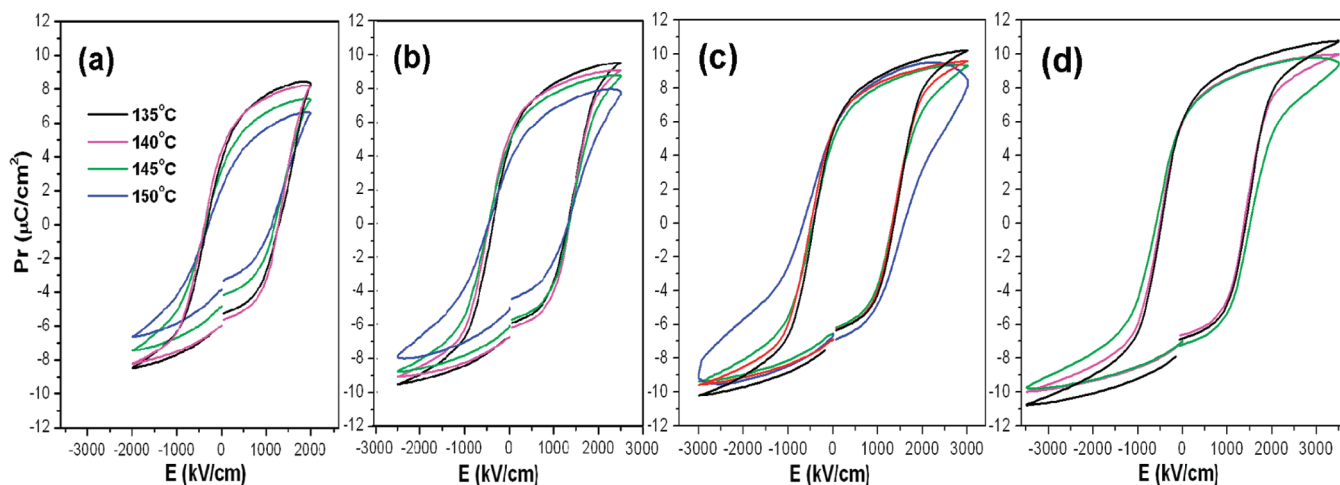


**Figure 4.** Parts (a), (b), (c), and (d) are the  $P-E$  loops of different 60 nm-thick P(VDF-TrFE) films on Al-coated Si obtained under a sequentially increasing electric field of 2000, 2500, 3000, and 3500 kV/cm, respectively.

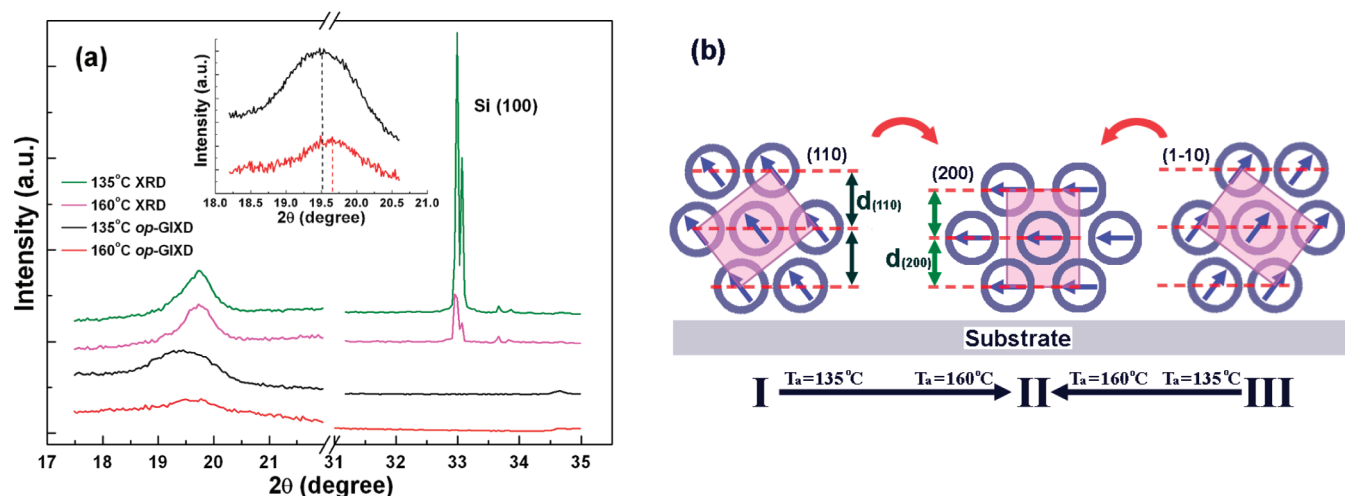


**Figure 5.** (a) XRD and op-GIXD patterns of 40 nm-thick 135 °C annealed granular film and 160 °C annealed LNN film on Al-coated Si. The profiles before and after the  $x$ -axis break have different intensity scales. The inset shows op-GIXD patterns under a much slower scan rate. (b) Illustration of three backbone packing status with the  $\{200\}$  or  $\{110\}$  plane families oriented parallel to the substrate. In the figure, the  $c$ -axis of the P(VDF-TrFE) lattice is perpendicular to the paper plane.

plane families parallel to the substrate (see Figure 5b). Interestingly, the intensity of the op-GIXD profile of the 160 °C annealed LNN film is shifted to higher  $2\theta$  as compared to that of the 135 °C annealed granular film, although their normal XRD patterns are very similar. The difference is clearer from the narrower range op-GIXD profiles shown in the inset, and such a feature was confirmed by repeated measurements. Note that P(VDF-TrFE) lattice has a tendency to orient with either the  $\{200\}$  or the  $\{110\}$  plane families parallel to the substrate due to the relatively lower surface energy, which results from their more dense chain packing than other planes.<sup>25</sup> In addition, the reported structure factor of the  $(110)$  plane is very slightly larger than that of the  $(200)$  plane in the quasi hexagonal lattice of the  $\beta$  phase with a VDF/TrFE mole ratio around 70/30.<sup>26,27</sup> Therefore, to explain the different op-GIXD profiles, it is speculated that the amount of crystallites that are preferentially oriented with their  $(200)$  planes parallel to the diffraction plane (slightly tilted away from the film plane) is relatively higher in the 160 °C

annealed film than in the 135 °C annealed film. If this is true, the  $b$ -axis should rotate to an average more perpendicular orientation (relative to the film surface) when  $T_a$  is increased from 135 to 160 °C, resulting in more  $(200)$  diffraction planes with a shorter interplane distance. Such an orientation change is schematically illustrated in Figure 5b. However, more complicated chain movement (see Figure 7) is necessary to account for the similarity of normal XRD profiles of the two films.

The aforementioned specific problems of the P(VDF-TrFE) films, for example, the overlapped  $(200)$  and  $(110)$  diffraction and the tendency to orient with the  $\{200\}$  or  $\{110\}$  plane families parallel to substrate, impose limitation to its lattice orientation analysis by using various XRD techniques if the lattice might exhibit a complicated cooperative movement. In IRRAS technique, the net absorption of p-polarized component (with transition dipole moments perpendicular to the film surface) is almost doubled due to the similar phase angle of the incident and reflected beams, while the absorption of the s-polarized

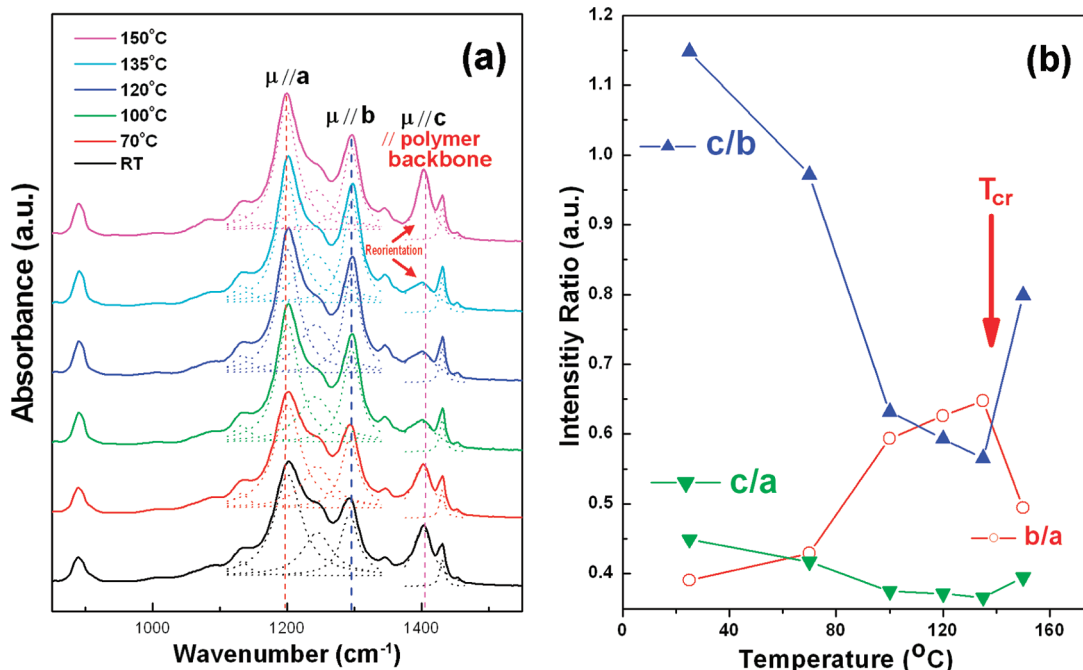


**Figure 6.** (a) IRRAS spectra of different 40 nm-thick P(VDF-TrFE) films on Au-coated Si. (b)  $T_a$  dependence of intensity ratio of the three strongest bands located at  $\sim 1200$ ,  $\sim 1290$ , and  $\sim 1400$   $\text{cm}^{-1}$ , whose intensities are denoted as  $a$ ,  $b$ , and  $c$ , respectively.

**Table 1. Assignments of the IR Absorption Peaks in the Crystallographic  $\beta$  Phase P(VDF-TrFE)<sup>a</sup>**

wavenumber	assignments	symmetry and orientation
890	r CH <sub>2</sub> coupled with $\nu_a$ CF <sub>2</sub> and r CF <sub>2</sub>	B2, $\mu \parallel a$ -axis
1185	$\nu_a$ CF <sub>2</sub> coupled with r CF <sub>2</sub>	B2, $\mu \parallel a$ -axis
1290	$\nu_s$ CF <sub>2</sub> coupled with $\nu_s$ CC and $\delta$ CCC	A1, $\mu \parallel b$ -axis
1400	$\omega$ CH <sub>2</sub> coupled with $\nu_a$ CC	B1, $\mu \parallel c$ -axis
1428	$\delta$ (CH <sub>2</sub> )	A1, $\mu \parallel b$ -axis

<sup>a</sup> The symbols  $\nu_a$  and  $\nu_s$  represent, respectively, antisymmetric and symmetric stretching modes.  $\delta$ , r, and  $\omega$  represent bending, rocking, and wagging modes, respectively.

component (with transition dipole moments parallel to the film surface) is nearly canceled out because of the  $\sim 180^\circ$  phase shift. Thus, only the transition dipole moments oriented perpendicularly to film surface are active, and the spectra can be interpreted in a straightforward manner. In the IRRAS spectra shown in Figure 6a, the peaks at  $\sim 885$  and  $\sim 1200$   $\text{cm}^{-1}$  are attributed to the vibrational modes parallel to the lattice  $a$ -axis. The vibrations corresponding to  $\sim 1290$  and  $\sim 1428$   $\text{cm}^{-1}$  and those corresponding to  $\sim 1400$   $\text{cm}^{-1}$  are parallel to the  $b$ -axis and the  $c$ -axis, respectively (see Table 1).<sup>28,29</sup> The most obvious change of the curves comes from the 1400  $\text{cm}^{-1}$  band, whose intensity shows a minimum at 135 °C. Because there are several IR-active vibration with differently oriented transition dipoles, the “relative intensity” method was used to quantitatively determine the lattice orientation.<sup>30</sup> The variation of the intensity ratio of the three strongest bands at  $\sim 1200$ ,  $\sim 1290$ , and  $\sim 1400$   $\text{cm}^{-1}$  derived by deconvoluting the peaks with Lorentzian functions is plotted in Figure 6b. Both  $c/a$  and  $c/b$  exhibit minimum values, while  $b/a$  shows a maximum at 135 °C (just below  $T_{cr}$ ). Because the absorption intensity is proportional to  $(\mu \cdot E)^2$ , where  $\mu$  and  $E$  refer to

the dipole moment and the IR electric field intensity, respectively, a higher intensity of a band means a relatively more perpendicular orientation of the corresponding axis in relation to the film surface. Therefore, the  $c/a$  and  $c/b$  curves in Figure 6b imply that the  $c$  axis (i.e., the polymer backbone) first gradually lies down with increasing  $T_a$ , and then shows an abrupt standing-up reorientation upon the formation of the LNN structure, as illustrated in Figure 7a. Meanwhile, the  $b/a$  curve in Figure 6b implies that the  $b$  axis shows exactly a contrary orientation change as illustrated in Figure 7b. The cooperative overall macromolecular orientation change can be schematically illustrated in Figure 7c through the movement of a unit cell in a three-dimensional ordination system, where the included angle between the  $b$  axis and the surface plane ( $\alpha$ ) is visualized by the projection of dipole on the film plane. The results give such relationships:  $\beta_2 > \beta_3 > \beta_1$  and  $\alpha_2 > \alpha_3 > \alpha_1$ . Because the ferroelectric response of the films is approximately proportional to  $\alpha$  if other influences are neglected, the  $T_a$  dependence of  $P_r$  shown in Figure 3d can be at least partly interpreted by the polymer orientation change, as reflected by the similar shape of the  $b/a$  curve in Figure 6b with that of the  $P_r$  curve in Figure 3d. The deterioration of ferroelectricity upon the formation of the needles is to a certain degree caused by the lying down dipole reorientation. Figure 7 also agrees well with Figure 5a: the rightward shift of the op-GIXD peak of the LNN film is caused by the increased amount of more densely packed (200) diffraction planes with the lying-down  $b$ -axis movement, while the simultaneous tilting of the backbone may have concealed this effect for the normal XRD patterns (but may not conceal the effect for the op-GIXD patterns), whose signal comes from the planes parallel to the substrate.

More information about the molecular orientation status can be derived from the backbone orientation of the as-cast film. It is well-known that the chains of solvent cast amorphous thin polymer films prefer to orient parallel to the film plane.<sup>13,31</sup> If this

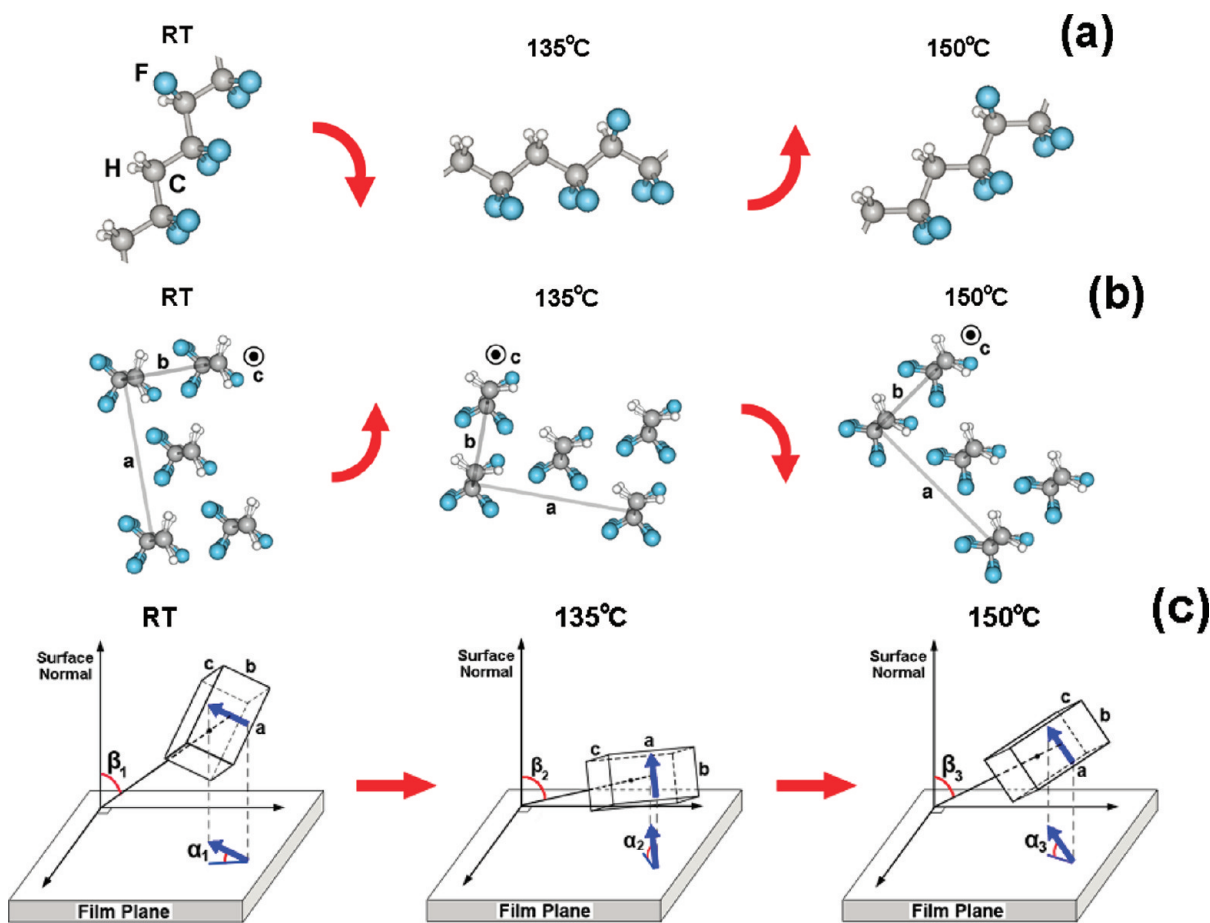


**Figure 7.** Schematic illustration of the P(VDF-TrFE) molecular orientation change at different  $T_a$  range. (a) The backbone orientation change. (b) The  $b$ -axis orientation change. (c) Cooperative overall lattice orientation change, where the blue arrows represent the dipole orientation, and a unit lattice cell is used for clarity.

is true for the as-cast RT P(VDF-TrFE) film sample, Figure 7 may suggest that the chains tend to lie further down upon thermal crystallization. Thus, the smaller  $c/a$  and  $c/b$  and larger  $b/a$  values of the 150 °C sample than those of the RT one imply that the polymer chains in the LNN film are still on average preferentially oriented parallel to the film plane, despite the abrupt standing-up chain movement upon the formation of needles. Furthermore, because IR spectra are not sensitive to the crystallinity, Figure 7 actually reflects the molecular orientation change of both crystalline and amorphous regions in the whole films. Moreover, a similar  $T_a$ -dependent molecular orientation variation as shown in Figure 7 was observed for films in the thickness range of 30–250 nm, despite a slight thickness-dependent orientation change similar to other polymer films.<sup>32,33</sup>

**Discussion of the Molecular Orientation Mechanisms.** During thermal crystallization, the randomly coiled chain segments reorganize to form a thermodynamically more stable, better-ordered structure, while in ultrathin films a great part of the conformational entropy has to be reduced and the resulting crystal has to obey strong constraints due to the linear connectivity of crystallizing units and the geometry confinement. Therefore, the lying down of  $c$ -axis at  $T_a < 135$  °C may have resulted from the initial chain segments aligned along the substrate plane, which could act as nuclei and induce more molecules to crystallize along the same direction. The simultaneous  $b$ -axis standing-up rotation is presumably related to the

preferential nucleation and growth of film on the energetically more favorable specific planes, for example, the {110} planes. A certain other unclear cause such as the interaction between the dipoles might also have an effect. The chain orientation change of melt crystallized polymer ultrathin films is much more complicated, and the underlying mechanisms are matters of debate.<sup>5,30,31</sup> An issue deserving more discussion is chain tilting in relation to the lamella plane, an important feature observed in a number of polymers, such as polypropylene<sup>34</sup> and polyethylenes,<sup>35</sup> etc. It was suggested that during crystallization, exclusion of “semi-ordered” chain segments outside the crystalline region imposes steric constraints, which could be reduced by chain tilting.<sup>36</sup> Tilted growth also allows better packing and enhanced space for the accommodation of disordered conformations.<sup>37</sup> Importantly, here tilted P(VDF-TrFE) chains in the LNN film ( $T_a > 140$  °C) can reconcile the edge-on lamellae morphology feature and the nonflat lying chain orientation of the needle grains. The different orientation of the granular and LNN films formed under different  $T_a$  may hence be rationalized by the competition between the chain attachment and detachment from the crystalline phase: nucleation from melt proceeds with highly mobile tilted chains as the building blocks, while at lower  $T_a$  it proceeds with nuclei mainly consisting of untilted chains.

**PFM Characterization and Nanoscale Polarization Switching Behavior.** In PFM characterization, a sine AC voltage signal

excites mechanical displacements in the sample via the converse piezoelectric effect, and the displacement is monitored locally with the AFM probe (see Figure 8). PFM amplitude (labeled as AM),

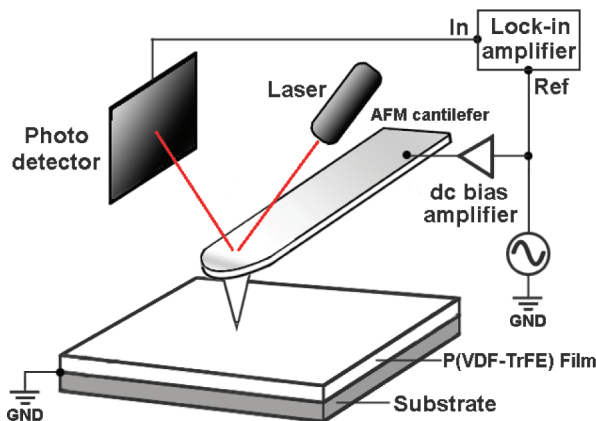


Figure 8. Schematic illustration of the PFM experimental setup.

phase (labeled as PH), and AFM topography images of a granular film and a LNN film are shown in Figures 9 and 10, respectively. For the 150 °C annealed LNN film sample, an area with a melt-like cluster (see Figure 10c) was selected to check its difference in piezoresponse in comparison with the needle grains. The PFM amplitude image of the 135 °C annealed granular film in Figure 9a shows irregularly shaped small bright regions of evident piezoresponse. The corresponding bright and dark regions in the phase image in Figure 9b represent domains with a polarization oriented away from (up) and toward (down) the substrate, respectively. These images are different from those obtained from films with pinholes annealed under similar conditions.<sup>38</sup> Magnified images of the region inside the white ellipses in Figure 9a and b are compared in Figure 9c. As indicated by the white arrows, the dark line between two white regions in Figure 9c shows an unpolarized domain wall, which corresponds to the boundary between two oppositely polarized domains in the phase image. The line between two domains with the same polarization, as indicated by the black arrow, is not present in the phase image. The ferroelectric domains show no

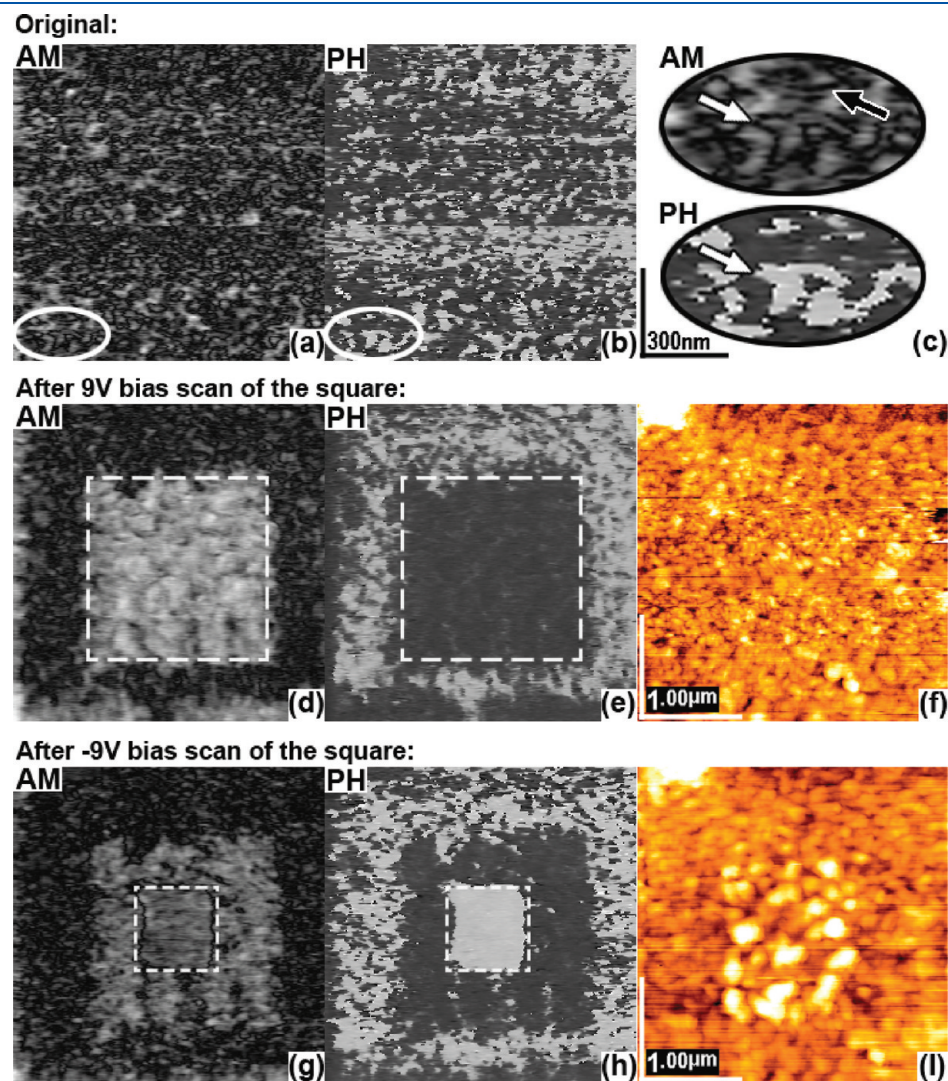
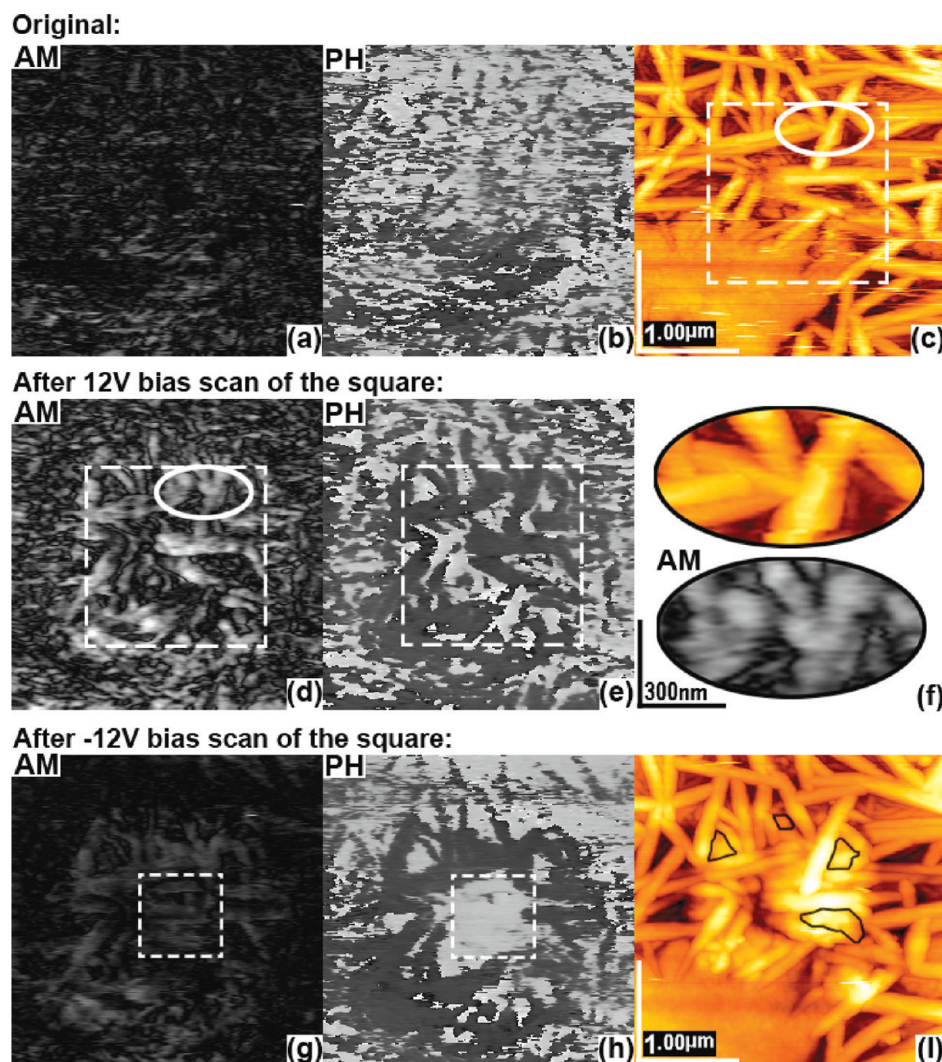


Figure 9. PFM and AFM images of 135 °C annealed 40 nm-thick granular film. (a) PFM amplitude image. (b) PFM phase image. (c) Comparison of magnified amplitude and phase images of an elliptic region as indicated in (a) and (b). Parts (d)–(f) are the PFM amplitude, PFM phase, and AFM images taken after a 9 V bias scan, respectively. Parts (g)–(i) are the PFM amplitude, phase, and AFM images taken after a -9 V bias scan, respectively. Except for (c), all images have the same size of 3  $\mu\text{m} \times 3 \mu\text{m}$ .



**Figure 10.** PFM and AFM images of 145 °C annealed 40 nm-thick LNN film. (a) PFM amplitude. (b) PFM phase. (c) Topography. Parts (d) and (e) are, respectively, the PFM amplitude and phase images taken after a 12 V bias scan. (f) Comparison of magnified AFM and PFM amplitude images of an elliptic region selected from (c) and (d), respectively. Parts (g)–(i) are the PFM amplitude, phase, and AFM images taken after a −12 V bias scan, respectively. Except for (c), all images have the same size of 3  $\mu\text{m} \times 3 \mu\text{m}$ .

correlation with the topography shown in Figure 9f. For the LNN film, similar PFM images can be observed, and there is still no strong correlation between the ferroelectric domains and the topography (see Figure 10a–c). An interesting feature of Figure 10a is that there may exist different ferroelectric domains with different piezoresponse in the same needle grain, as reflected by the different darkness, implying that different regions in the same needle grain may have different dipole orientation angle. Comparing Figure 10a and c, one can also see that a part of the melt-like cluster still shows a piezoresponse similar to other regions in the film. It seems to consist of small crystallites and a surrounding amorphous matrix. Combined with previous results, a layered-lamellae model with different chain tilting angle as schematically illustrated in Figure 11 can be proposed for the LNN film.

For the polarization switching study (Figures 9d and 10d), first, a  $1.7 \mu\text{m} \times 1.7 \mu\text{m}$  square was scanned with a DC bias for 256 lines at 0.2 line/s, and then PFM images of the total  $3 \mu\text{m} \times 3 \mu\text{m}$  area were recorded. Second, a smaller  $600 \text{ nm} \times 600 \text{ nm}$  square was poled in the opposite direction by a negative DC bias,

and then PFM imaging was repeated. For the granular film, the polarization of the 9 V bias scanned region (indicated by the large dash square in Figure 9d and e) was almost completely switched from the original state. In sharp contrast, for the LNN film, the polarization of the area scanned with even a higher DC bias of 12 V shown in Figure 10d and e could still not be uniformly switched. For both films, the morphology tested after the positive bias scan, as shown in Figures 9f and 10f, shows no obvious change, even though the dipoles perpendicular to the polymer chains should have been rotated. Comparing Figure 10d with c, one can find that the polarization domains prefer to grow along the needles and are largely confined within the needles. Thus, the needle shape appears to be “printed” on the PFM images. To see more details, we compare in Figure 10f the magnified topography and PFM amplitude images taken from the elliptic region in Figure 10c and d. It can be seen that the dipoles of the needle covered area were switched, while the area between the needles consists of both active and inactive regions. As indicated by the dash squares (Figure 9g and h), a second −9 V bias scan caused a homogeneous upward polarized region with relatively uniform

piezoresponse. The distorted square shape is due to the drift of the sample during scan. In contrast, for the LNN film, Figure 10g and h indicates that a  $-12$  V bias scan could still not induce a homogeneously polarized square. The distorted square shape again indicates that the domain switching is constrained by the needle geometry. The results imply a much lower writing resolution of the LNN film than that of the granular film upon

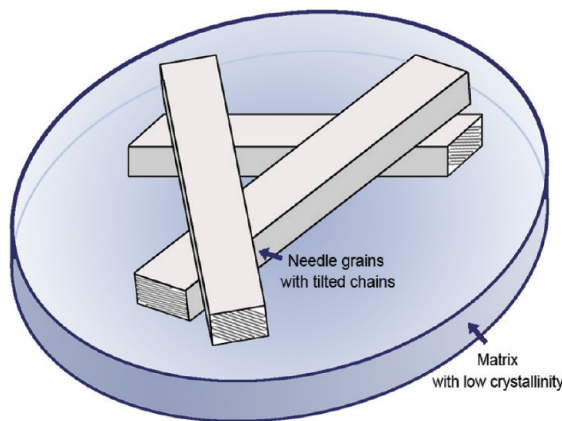


**Figure 11.** Schematic illustration of the layered tilted chain lamella structure model for the LNN film, where the chains in different lamellae have different tilting angles.

electric polarization. The weaker piezoresponse as reflected by the darker color of Figures 9g and 10g, respectively, than that of Figures 9d and 10d reveals an evident “imprint” effect in both films under test. This may be ascribed to the internal field generated by negative charges trapped at the interface.

The morphology of both films was modified after the negative bias scan (Figures 9i and 10i). This is not related to the polarity of the voltage, but related to the longer dwelling time of the tip, because the negative scan was performed on a smaller region with the same frequency. Actually, with the same tip dwelling time, the same modification effect was observed for both negative and positive bias. For the granular film, some small dots were produced after the  $-9$  V bias scan. The problem of morphology modification is much more serious in the LNN film. A square island induced by a  $-12$  V bias scan appears (Figure 10i). Interestingly, by comparing Figures 10c and i, one can find that more “needles”, as denoted by the black curves, appear among the original needles. These new grains seem to be “lifted” by the strong electric field. It was reported that the grain orientation in P(VDF-TrFE) film could be modified by contact-mode AFM, which might impose mechanical stress.<sup>21</sup> The larger modification area than the bias scanning area in Figure 9i and the new “grains” that appeared after the  $-12$  V bias scanning in Figure 10i indicate that the morphology change after polarization switching in this study should be to a large degree related to the electric interaction between the AFM tip and the polymer. The results indicate

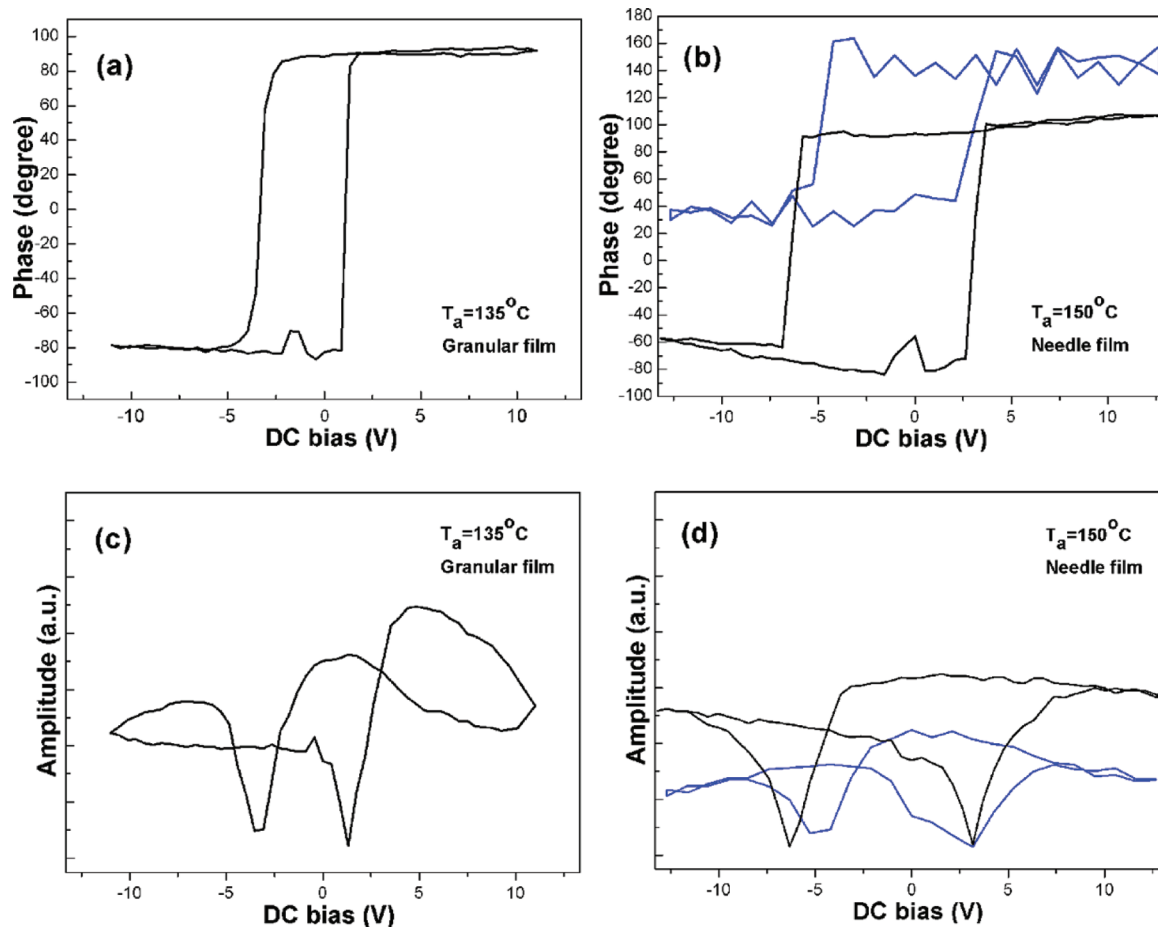


**Figure 12.** Local ferroelectric loops of two typical 40 nm-thick films deposited on Pt-coated Si. Parts (a) and (b) are the phase loops. Parts (c) and (d) are the amplitude loops, and the two figures have the same vertical scale.

that morphology change after repeated polarization switching is an important issue for practical fabrication of P(VDF-TrFE)-based ferroelectric memories. This may be alleviated by using suitable writing voltage and speed (see Figure 9f). The microscopic polarization switching results reveal that, in addition to the macromolecular orientation change, other causes of the smaller  $P_r$  of the LNN film than that of the granular film are its structural inhomogeneity and the domain-constraining effect of the large needle grains.

**Local Ferroelectric Hysteresis Loops.** In local microscopic ferroelectric loop measurement, a DC bias voltage was superimposed on a driving AC voltage, and the electromechanical vibration of the sample in the form of  $A \cos \varphi$  was detected by a lock-in amplifier. The amplitude  $A$  is related to the piezoelectric response, and the phase shift  $\varphi$  is dependent on the polarization direction.<sup>39</sup> For the granular film, relatively well-shaped loops could be repeatedly obtained in a randomly selected point with a driving voltage of  $\sim 10$  V. Typical loops plotted in the form of phase  $\varphi$  and amplitude  $A$  as a function of the DC voltage are shown in Figure 12a and c, respectively. The shift of the loop along the voltage axis arises from the asymmetry of the tip/film/bottom electrode configuration. In contrast, for the LNN film even under a higher driving voltage of about 13 V, well-shaped local ferroelectric loops could be obtained only on some needle grains, and the loops (Figure 12b and d) exhibit quite different amplitude, phase, and coercive field values. Occasionally, a loop with a very high phase shift (the upper loop in Figure 12b) was obtained. The origin of such a high phase shift is unclear. A tentative explanation is that the large roughness or plasticity of the needle-like structure may have caused the high phase shift. Also, local ferroelectric loops were not obtained on the regions between the grains. In addition, by comparing Figure 12b and d, we also find that the 135 °C annealed granular film shows relatively larger amplitude signal than that of the LNN film. Thus, agreeing well with the results shown in Figures 3, 4, 9, and 10, these phenomena confirm the better ferroelectric properties of the 135 °C annealed granular film than those of the LNN films, despite the lower crystallinity of the former.

## CONCLUSIONS

The cooperative molecular orientation, macroscopic ferroelectric properties, and nanoscale polarization switching behaviors of ultrathin P(VDF-TrFE) films annealed at different temperatures were systematically investigated. The films showed a distinct small-granule toward LNN morphology transition at a  $T_{cr}$  of 140 °C. Below  $T_{cr}$ , the crystallinity and  $P_r$  of the films gradually increased with  $T_a$ . However, above  $T_{cr}$ , much rougher and leakier films with deteriorated  $P_r$  were formed. By using XRD, op-GIXD, and IRRAS techniques, details of the thermally induced molecular orientation change were derived. With increasing  $T_a$ , the P(VDF-TrFE) backbone first lay more parallel to the substrate, then exactly at  $T_{cr}$ , the polymer backbone showed an interesting standing-up reorientation, while the polarization axis underwent just opposite orientation and reorientation. The orientation change was interpreted by the competition between the chain attachment and detachment from the crystalline phase. PFM revealed that polarization reversal in the LNN film could be confined within the needle grains, and different regions in the same needle grain might have different dipole orientation. A layered-lamellae model with different chain tilting degree was proposed to interpret the structural characteristics of the LNN

film. The results imply that a higher crystallinity does not necessarily lead to a better ferroelectric performance. The molecular orientation and film homogeneity are also important in controlling the film properties. The results may shed some light on the understanding of the intercorrelation among the thermal crystallization, the microstructural characteristics, and the macroscopic performance of ultrathin P(VDF-TrFE) films.

## AUTHOR INFORMATION

### Corresponding Author

\*E-mail: guodong99@tsinghua.org.cn, dong.guo@mail.ioa.ac.cn.

## ACKNOWLEDGMENT

This work was supported by the Competence Centre for Materials Science and Technology (CCMX) of Switzerland. Part of the work was done within the MIND network of excellence on Piezoelectrics (EU FP6 funded program). We thank Dr. Terrettaz Samuel and Mr. Condemi Enrico for their help in IRRAS measurements. D.G. also thanks the “Bairen Programme” of the Chinese Academy of Sciences for its financial support.

## REFERENCES

- (1) Bauer, S. *J. Appl. Phys.* **1996**, *80*, 5531–5558.
- (2) Kusuma, D. Y.; Nguyen, C. A.; Lee, P. S. *J. Phys. Chem. B* **2010**, *114*, 13289–13293.
- (3) Ducharme, S.; Reece, T. J.; Othon, C. M.; Rannow, R. K. *IEEE Trans. Device Mater. Reliab.* **2005**, *5*, 720–735.
- (4) Stolichnov, I.; Riester, S. W. E.; Trodahl, H. J.; Setter, N.; Rushforth, A. W.; Edmonds, K. W.; Campion, R. P.; Foxon, C. T.; Gallagher, B. L.; Jungwirth, T. *Nat. Mater.* **2008**, *7*, 464–467.
- (5) Sommer, J. U.; Reiter, G. *Thermochim. Acta* **2005**, *432*, 135–147.
- (6) Zhang, Q. M.; Xu, H. S.; Fang, F.; Cheng, Z. Y.; Xia, F.; You, H. *J. Appl. Phys.* **2001**, *89*, 2613–2616.
- (7) Furukawa, T.; Nakajima, T.; Takahashi, Y. *IEEE Trans. Dielectr. Electr. Insul.* **2006**, *13*, 1120–131.
- (8) Naber, R. C. G.; Blom, P. W. M.; Marsman, A. W.; Leeuw, D. M. *Appl. Phys. Lett.* **2004**, *85*, 2032–2034.
- (9) Fujisaki, S.; Ishiwara, H.; Fujisaki, Y. *Appl. Phys. Lett.* **2007**, *90*, 162902.
- (10) Alamo, R. G.; Mandelkern, L.; Stack, G. M.; Krohnke, C.; Wegner, G. *Macromolecules* **1994**, *27*, 147–156.
- (11) Hikosaka, M.; Amano, K.; Rastogi, S.; Keller, A. *Macromolecules* **1997**, *30*, 2067–2074.
- (12) Sakai, Y.; Imai, M.; Kaji, K.; Tsuji, M. *Macromolecules* **1996**, *29*, 8830–8834.
- (13) Jones, R. L.; Kumar, S. K.; Ho, D. L.; Briber, R. M.; Russell, T. P. *Nature (London)* **1999**, *400*, 146–149.
- (14) Tsutsumi, N.; Yoda, S.; Sakai, W. *Polym. Int.* **2007**, *56*, 1254–1260.
- (15) El-Hami, K.; Matsushige, K. *J. Appl. Polym. Sci.* **2005**, *96*, 1410–1413.
- (16) Park, Y. J.; Kang, S. J.; Park, C.; Kim, K. J.; Lee, H. S.; Lee, M. S.; Chung, U.; Park, I. J. *J. Appl. Phys. Lett.* **2006**, *88*, 242908.
- (17) Chen, X. Q.; Yamada, H.; Terai, Y.; Horiuchi, T.; Matsushige, K.; Weiss, P. S. *Thin Solid Films* **1999**, *353*, 259–263.
- (18) Rodriguez, B. J.; Jesse, S.; Kalinin, S. V.; Kim, J.; Ducharme, S.; Fridkin, V. M. *Appl. Phys. Lett.* **2007**, *90*, 122904.
- (19) Gysel, R.; Stolichnov, I.; Tagantsev, A. K.; Setter, N.; Mokry, P. *J. Appl. Phys.* **2008**, *103*, 084120.
- (20) Fukuma, T.; Kobayashi, K.; Horiuchi, T.; Yamada, H.; Matsushige, K. *Jpn. J. Appl. Phys.* **2000**, *39*, 3830–3833.
- (21) Kimura, K.; Kobayashi, K.; Yamada, H.; Horiuchi, T.; Ishida, K.; Matsushige, K. *Appl. Phys. Lett.* **2003**, *82*, 4050–4052.

- (22) Kikkawa, Y.; Abe, H.; Fujita, M.; Iwata, T.; Inoue, Y.; Yoshiharu, D. *Macromol. Chem. Phys.* **2003**, *204*, 1822–1831.
- (23) Jackson, C. L.; McKenna, G. B. *J. Chem. Phys.* **1990**, *93*, 9002–9011.
- (24) Fonest, J. A.; Mattsson, J. *Phys. Rev. E* **2000**, *61*, R53–R56.
- (25) Ohigashi, H.; Omote, K.; Gomyo, T. *Appl. Phys. Lett.* **1995**, *66*, 3281–3283.
- (26) Urayama, K.; Tsuji, M.; Neher, D. *Macromolecules* **2000**, *33*, 8269–8279.
- (27) Ikeda, S.; Yuki, T. *Polymer* **2002**, *43*, 4783–4789.
- (28) Kobayashi, M.; Tashiro, K.; Tadokoro, H. *Macromolecules* **1975**, *8*, 158–171.
- (29) Petzelt, J.; Legrand, J. F.; Pacesova, S.; Kamba, S. *Phase Transitions* **1988**, *12*, 305.
- (30) Debe, M. K.; Kam, K. K. *Thin Solid Films* **1990**, *186*, 289.
- (31) Yethiraj, A.; Hall, C. K. *J. Chem. Phys.* **1991**, *95*, 8494–8506.
- (32) Hu, Z. J.; Huang, H. Y.; Zhang, F. J.; Du, B. Y.; He, T. B. *Langmuir* **2004**, *20*, 3271–3277.
- (33) Reiter, G.; Sommer, J. U. *J. Chem. Phys.* **2000**, *112*, 4376–4383.
- (34) Cao, Y.; Horn, R. M. V.; Tsai, C. C.; Graham, M. J.; Jeong, K. U.; Wang, B. J.; Auriemma, F.; Rosa, C. D.; Lotz, B.; Cheng, S. Z. D. *Macromolecules* **2009**, *42*, 4758–4768.
- (35) Lotz, B.; Cheng, S. Z. D. *Polymer* **2005**, *46*, 577–610.
- (36) Frank, F. C. *Faraday Discuss. Chem. Soc.* **1979**, *68*, 7.
- (37) Keith, H. D.; Padden, F. J. *Macromolecules* **1996**, *24*, 7776–7786.
- (38) Choi, Y. Y.; Hong, J.; Hong, S.; Song, H.; Cheong, D. S.; No, K. *Phys. Status Solidi* **2010**, *4*, 94–96.
- (39) Kalinin, S. V.; Bonnell, D. A. *Phys. Rev. B* **2002**, *65*, 125408.